applied sciences

MDPI

Article

Thermal–Mechanical FEM Analyses of a Liquid Rocket Engines Thrust Chamber

Michele Ferraiuolo [1,*], Michele Perrella [2], Venanzio Giannella [3] and Roberto Citarella [3]

[1] Italian Aerospace Research Center (CIRA), Via Maiorise snc, 81043 Capua, Italy
[2] Department of Chemical, Materials and Production Engineering, University of Naples "Federico II", 80125 Naples, Italy; michele.perrella@unina.it
[3] Department of Industrial Engineering, University of Salerno, 84084 Fisciano, Italy; vgiannella@unisa.it (V.G.); rcitarella@unisa.it (R.C.)
* Correspondence: m.ferraiuolo@cira.it

Abstract: The Italian Ministry of University and Research (MIUR) funded the HYPROB Program to develop regeneratively cooled liquid rocket engines. In this type of engine, liquid propellant oxygen–methane is used, allowing us to reach very good performances in terms of high vacuum specific impulse and high thrust-to-weight ratio. The present study focused on the HYPROB final ground demonstrator, which will be able to produce a 30 kN thrust in flight conditions. In order to achieve such a thrust level, very high chamber pressures (up to 50 bar) and consequently high thermal fluxes and gradients are expected inside the thrust chamber. Very complex and high-fidelity numerical FEM models were adopted here to accurately simulate the thermal–mechanical behavior of the thrust chamber cooling channels, accounting for plasticity, creep, and low-cycle fatigue (LCF) phenomena. The aim of the current work was to investigate the main failure phenomena that could occur during the thrust chamber's service life. Results demonstrated that LCF is the main cause of failure. The corresponding number of loading cycles to failure were calculated accordingly.

Keywords: liquid rocket engine; finite element method; simulation; thermal stress; low-cycle fatigue; creep; plasticity

check for updates

Citation: Ferraiuolo, M.; Perrella, M.; Giannella, V.; Citarella, R. Thermal–Mechanical FEM Analyses of a Liquid Rocket Engines Thrust Chamber. *Appl. Sci.* **2022**, *12*, 3443. https://doi.org/10.3390/app12073443

Academic Editor: Maria Grazia De Giorgi

Received: 4 February 2022
Accepted: 24 March 2022
Published: 28 March 2022

1. Introduction

The aim of the HYPROB Program is to design, manufacture, and test a ground demonstrator of a liquid rocket engine employing liquid methane and liquid oxygen. Such a propulsion technology may cover a wide range of aerospace propulsion systems, from launcher main stages up to small thrusters. When the requested levels of thrust are relatively high, heavy heat fluxes and high chamber pressures are expected in the combustion chamber. Therefore, active cooling techniques can be used to keep the selected materials at acceptably low temperature values. The thrust chamber considered in the current investigation comprised an inner structure made of a CuCrZr alloy, and an external cold structure made of electrodeposited nickel. Methane, before being injected as fuel into the combustion chamber, also acts as a coolant fluid flowing through axial cooling channels, so as to partially remove heat from the inner structures, see Figure 1. Even though temperature levels are lowered with such a cooling process, very high thermal gradients occur within the structure, separating the hot gas from the cooling channels, where the fuel temperature is considerably lower.

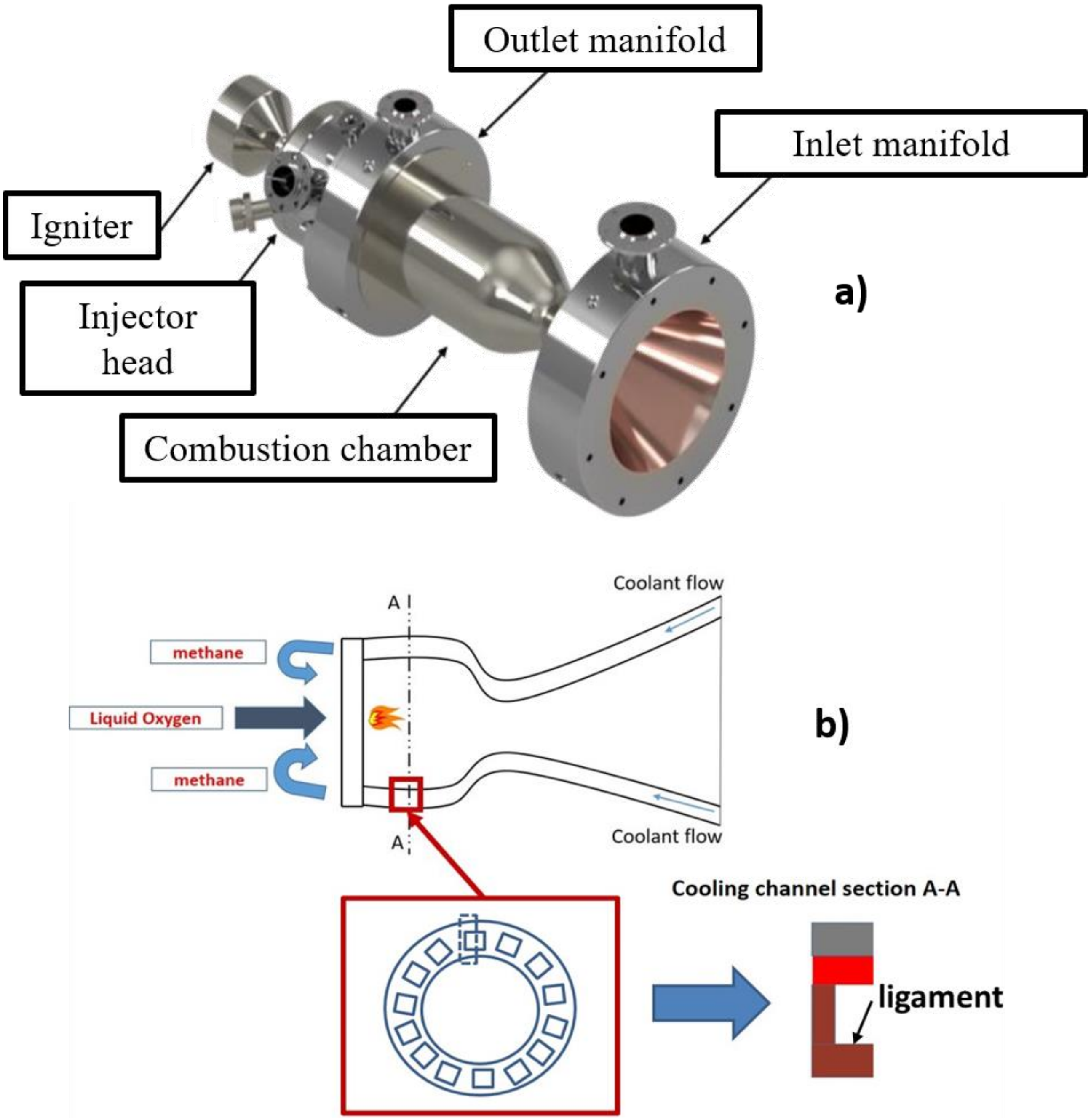

Figure 1. Rocket engine thrust chamber (**a**) and related functional scheme (**b**).

Several works can be found in the literature regarding the thermal–mechanical behavior of liquid rocket engines thrust chambers under cyclic loading conditions. These have demonstrated that plasticity effects should be modeled by means of both isotropic and kinematic hardening models. Additionally, a nonlinear kinematic hardening model should be adopted to simulate shakedown and ratcheting phenomena [1–3]. In particular, when employing the Chaboche kinematic hardening model [4], at least three nonlinear hardening models should be considered to simulate ratcheting behavior properly, i.e., the progressive plastic strain accumulation during cycling [5]. Other researchers also demonstrated that low-cycle fatigue (LCF) and creep can be the main possible causes of failure, in turn, highlighting the need to accurately investigate these phenomena [6–8]. Creep effects can be dominant when temperatures and stresses reach significantly high values [9–12]. Even if Norton secondary creep law [13] has been usually considered for these applications in literature, the authors have chosen to adopt a more complete creep model taking account of both primary and secondary creep effects through combined time hardening rules. With regard to the LCF phenomenon, uniaxial fatigue criteria are usually adopted for these kind of applications, since circumferential plastic strains are the dominant contributors with respect to the radial and axial ones. However, authors have adopted a critical plane approach, namely, the Wang-Brown criterion [14], to consider the effects of the multi-axiality of the stress-strain fields and non-proportionality of the loading conditions, because the influence of multiaxial and non-proportional loading effects is not negligible when evaluating the service life of these kind of structures. The latest advances of numerical methods, such as the finite element method (FEM), allowed us to study these complex structures and loading conditions, reducing the burden of expensive experimental tests.

The aim of the present work was to conduct a numerical investigation on the 3D thermal–mechanical behavior of a cooling channel of the thrust chamber by employing state-of-the-art numerical FEM models. This allowed us to take account of plasticity, creep, and LCF phenomena simultaneously. These analyses were conducted by means of the FEM code ANSYS. A preliminary work involving the same case study and concerning the adoption of global/local approaches can be found in [15]. As a continuation of [15], in the present work, plasticity effects were studied adopting the von Mises yield criterion, Prandtl-Reuss flow rule, and both isotropic and non-linear Chaboche kinematic hardening models. Multiaxial LCF evaluations were carried out by employing experimental fatigue test data available in literature [16]. Finally, the combined time hardening creep model was adopted to simulate primary and secondary creep stages [17]. A cumulative damage model, considering the effects of plastic instability (thermal ratcheting), creep, and fatigue, was employed so as to evaluate the number of cycles up to failure.

The rest of this document can be summarized as follows. Section 2 describes the adopted mathematical models with the related governing equations. Section 3 describes the numerical FEM models. Section 4 describes the thermal–mechanical loading conditions, whereas Section 5 presents the life prediction models adopted here. Finally, results are presented and discussed in Section 6, whilst the concluding remarks are reported in Section 7.

2. Mathematical Model

A weak coupling between thermal and structural problems was considered, so that temperature distribution affects the strain/stress fields but not vice-versa (see Figure 2). This is a common practice for these kinds of thermal–mechanical simulations since it allows one to strongly reduce the computational efforts without appreciable detrimental effects on accuracy [18–23]. In particular, the body temperatures calculated by means of a thermal transient analysis were transferred to a static non-linear structural analysis, where strain and stress fields were evaluated. Finally, the stress-strain fields were employed for the life prediction assessment, so as to eventually estimate the thrust chamber service life.

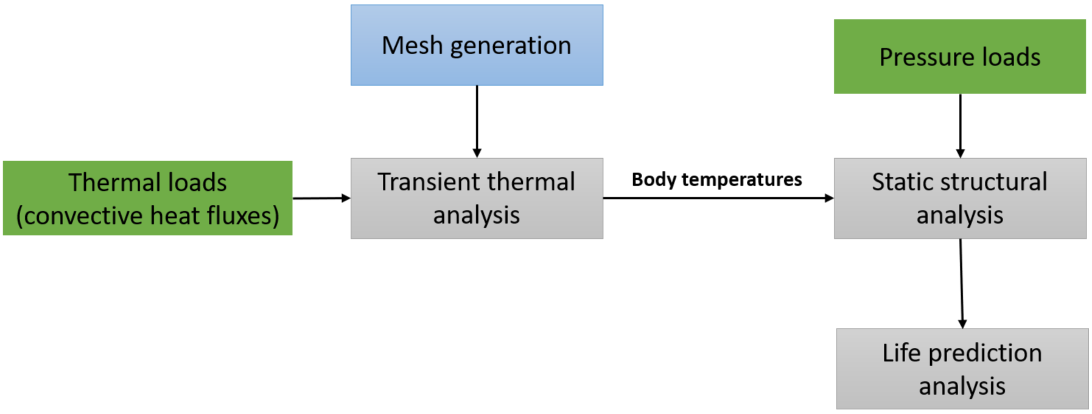

Figure 2. Workflow of the thermal–mechanical FEM analyses.

2.1. Thermal Model

Transient non-linear thermal analyses of the cooling channels were performed. The thermal problem was nonlinear because of the temperature-dependent material properties that were considered. The associated heat conduction problem is governed by the following differential equation [24,25]:

$$\nabla^2 T = \frac{1}{a}\frac{\partial T}{\partial \theta} \tag{1}$$

where a is the thermal diffusivity, T is the temperature, and θ is the time. Continuity of temperature and heat fluxes at the interface between chamber layers, made of CuCrZr alloy, electroformed copper, and electroformed nickel, were enforced through the following equations:

$$k_i \frac{\partial T_i}{\partial n} = k_j \frac{\partial T_j}{\partial n} \tag{2}$$

$$T_i = T_j \tag{3}$$

where i and j represent two generic materials in contact, k is the thermal conductivity, and n is the direction of the heat flow. Convective boundary conditions were applied to the hot gas side and to surfaces wetted by the coolant flow:

$$-k\frac{\partial T}{\partial n} = h\cdot(T_w - T_\infty) \tag{4}$$

where h is the convective heat transfer coefficient, T_w is the wall temperature, and T_∞ is the adiabatic wall temperature.

2.2. Structural Model

2.2.1. Plasticity

The equilibrium equation was combined with compatibility equations, constitutive laws, and the relationship between temperature variation and strain tensor. The temperature variation was evaluated with respect to a reference temperature at which no thermal strain was present. The total strain tensor ε can be decomposed into:

$$\varepsilon_{ij} = \varepsilon_{ij}^{el} + \varepsilon_{ij}^{pl} \tag{5}$$

where ε_{ij}^{el} and ε_{ij}^{pl} represent the elastic and plastic components of ε, respectively. Plasticity was modeled through the von Mises yield surface criterion, Chaboche kinematic hardening rule, a multilinear isotropic hardening model, and a Prandtl-Reuss flow rule, while creep phenomena were modeled by means of a combined time hardening law. A detailed description of the characteristics of the present viscoplastic model in comparison to other ones can be found in [11]. Materials subjected to cyclic loading harden both kinematically and isotropically. The multilinear isotropic model parameters were obtained by extrapolating data from the experimental stabilized stress vs. plastic strain curves at different temperatures for CuCrZr materials [15]. The Chaboche kinematic hardening model with three back stresses (each one corresponding to the Armstrong–Frederick nonlinear model) was chosen in order to consider the effects of kinematic hardening (see Figure 3) [26].

The total backstress tensor α can be expressed as follows:

$$\alpha = \frac{\Delta\sigma}{2} - \sigma_0 = \sum_{i=1}^{3} \frac{C_i}{\gamma_i}\left[\left(1 - \exp\left(-\gamma_i * \varepsilon_{pl}\right)\right)\right] \tag{6}$$

where C_i and γ_i are material parameters and σ_0 is the yield surface size. The calibration of the six coefficients (C_i, γ_i) was performed using a single stabilized stress–strain hysteresis loop for each temperature value [4]. This data elaboration was performed by means of the MATLAB "Curve Fitting" Toolbox [27] that allowed us to write custom equations adopted in combination with the nonlinear least square method. The corresponding coefficient of determination R^2 is equal to 0.98, where R^2 is evaluated as follows:

$$R^2 = 1 - \frac{\sum_i (y_i - f_i)^2}{\sum_i (y_i - \overline{y})^2} \tag{7}$$

where y_i are the original experimental data, f_i are the predicted values, and $\overline{y}$ is the mean of the experimental data set [28].

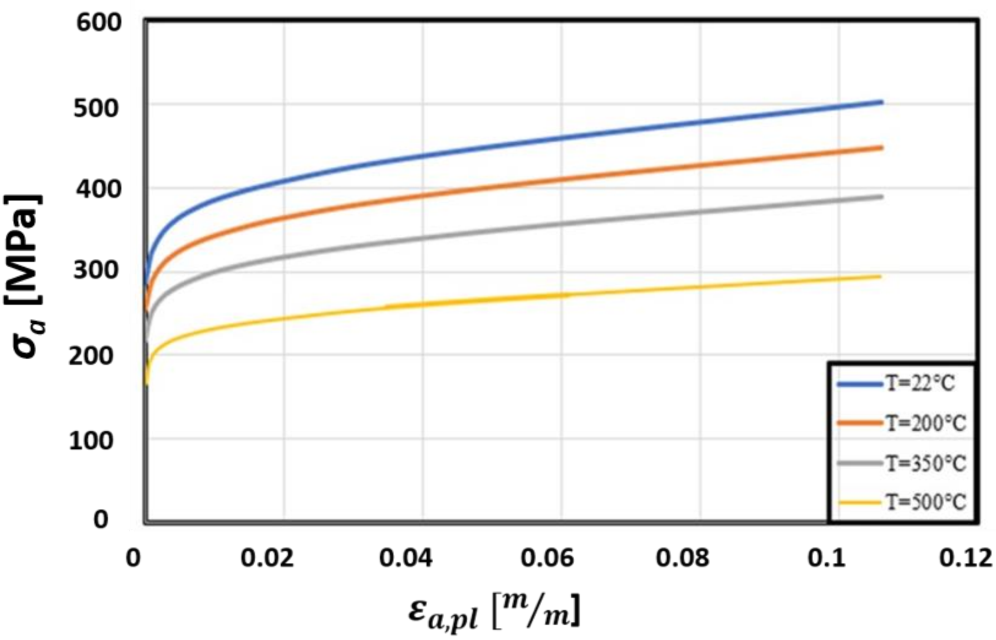

Figure 3. Temperature-dependent stress-strain curves for CuCrZr [16].

2.2.2. Creep

The creep phenomenon was analyzed by means of the "combined time hardening" model that describes both primary and secondary creep stages [17]. Such a model incorporates both time hardening and the Norton model. As time increases, the influence of time hardening component becomes irrelevant, while the Norton model for the secondary creep regime starts to be dominant. The material viscous behavior as a function of temperature was governed by the Arrhenius term. The combined time hardening model can be described through the following relationship:

$$\varepsilon_{cr} = \frac{D_1 \sigma^{D_2} t^{D_3+1} e^{-\frac{D_4}{T}}}{D_3 + 1} + D_5 \sigma^{D_6} t e^{-\frac{D_7}{T}} \tag{8}$$

Material coefficients $D_1, \ldots, D_7$ are taken from the work of Li et al. [10], and are listed into Table 1.

Table 1. Material coefficients for combined time hardening law, where stress is expressed in MPa, time in s, and temperature in K [10].

D_1	D_2	D_3	D_4	D_5	D_6	D_7
6.05×10^{10}	3	−0.92	23,695	2.82×10^{-22}	14	23,695

3. Numerical Model Description

Since the maximum heat flux values from the combustion chamber are expected in the throat, a local model of the throat region of the thrust chamber was examined in order to save the computation time required to investigate the whole chamber, see Figures 4 and 5.

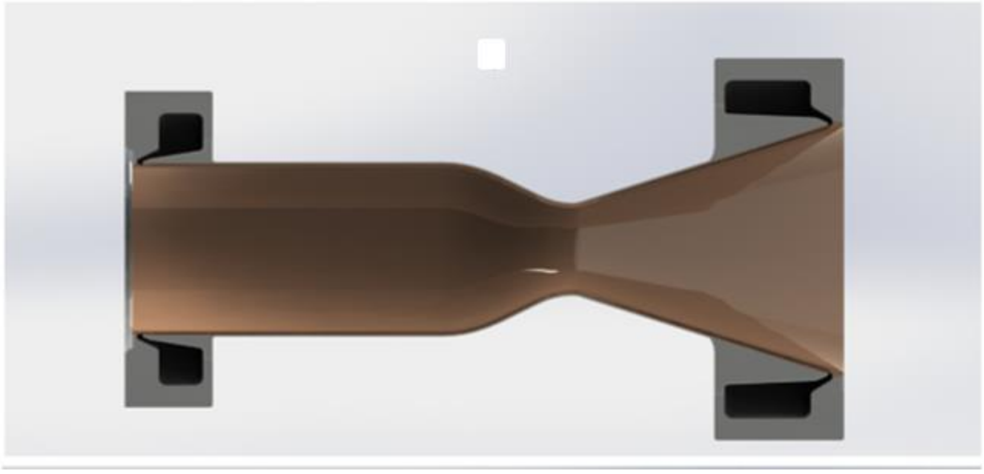

Figure 4. Thrust chamber geometry.

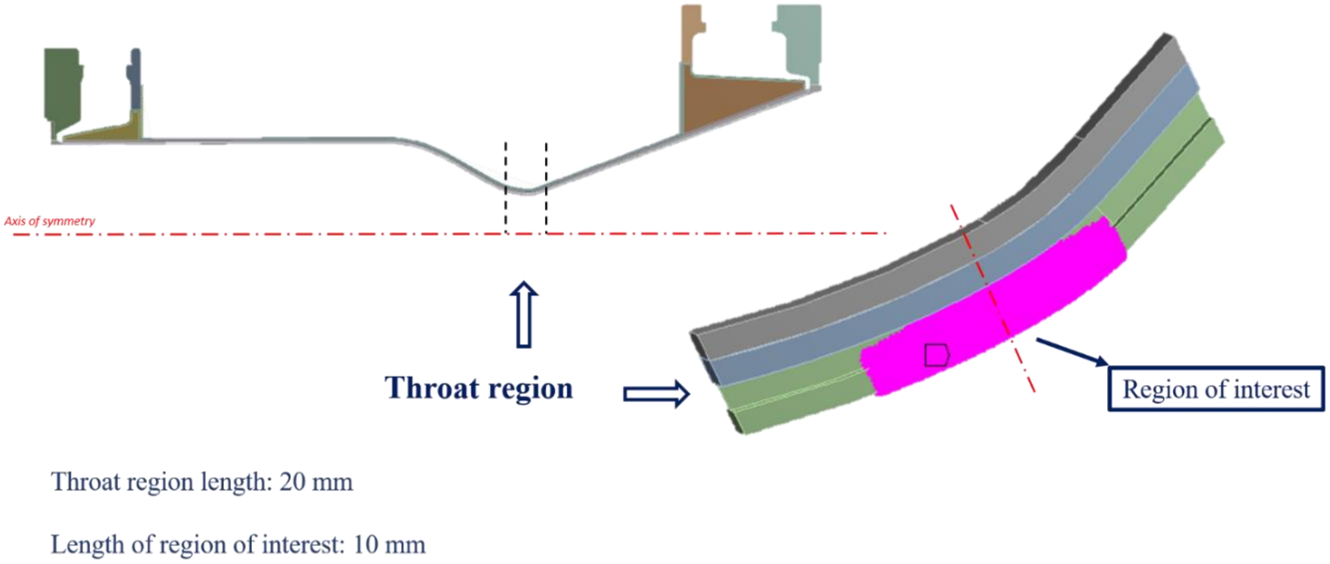

Throat region length: 20 mm

Length of region of interest: 10 mm

Figure 5. Regions of interest numerically analyzed.

Only a half-cooling channel was modeled, thus taking advantage of the symmetry. Cyclic symmetry boundary conditions were enforced at the two cut surfaces, so as to simulate the whole 360° of the chamber. Figure 6 shows a section of the cooling channel. Figure 5 shows the position of the throat region, where heat transfer coefficients of coolant and hot gases reach their maximum values. The region of interest was chosen as being sufficiently far from the end sections of the models in order to reduce the impact of the approximations caused by pre-defined boundary conditions (not obtained by a rigorous submodeling approach) on the cut surfaces (see Figure 5); here, the aim was to prove the effectiveness of the procedure, rather than strictly forecasting the working conditions.

The combustion chamber comprises three materials, as shown in Figure 6:

- CuCrZr alloy, in the region in contact with the coolant and the hot gases;
- a thin layer of electrodeposited oxygen-free, high-thermal conductivity copper (OFHC);
- a layer of electrodeposited nickel to provide adequate stiffness to the chamber.

Tables 2–7 summarize the physical and mechanical properties of the copper alloy (CuCrZr), the electrodeposited oxygen-free, high-thermal conductivity copper (OFHC), and nickel [15].

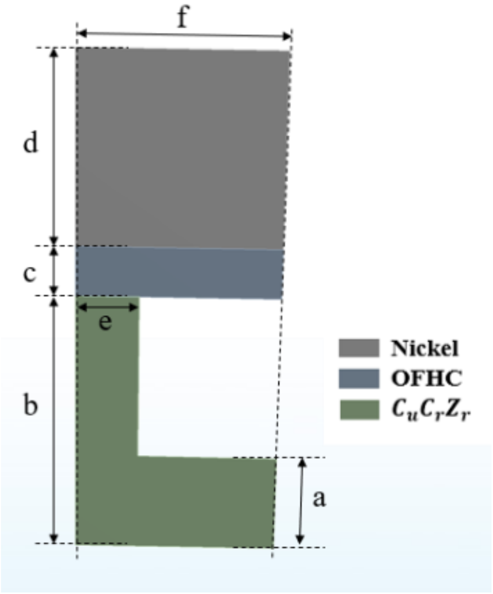

Figure 6. Cooling channel section.

Table 2. Physical and thermal properties of CuCrZr [16].

Temperature [K]	Mass Density $[\mathrm{kg/m^3}]$	Thermal Conductivity [W/mK]	Specific Heat [J/kgK]	Thermal Expansion Coefficient [1/K]
300	8933	320	390	15.7×10^{-6}
600	8933	290	390	17.9×10^{-6}
900	8933	255	400	18.7×10^{-6}

Table 3. Mechanical properties of CuCrZr.

Temperature [K]	Young's Modulus E [GPa]	Poisson's Ratio ν [-]	Yield Stress [MPa]	Ultimate Tensile Strength [MPa]
300	130	0.3	433.9	477.9
500	106	0.3	383.3	402.9
700	87	0.3	313	329.4
900	44	0.3	156.3	174.5

Table 4. Physical properties of electrodeposited OFHC.

Temperature [K]	Mass Density $[\mathrm{kg/m^3}]$	Thermal Conductivity [W/mK]	Specific Heat [J/kgK]	Thermal Expansion Coefficient [1/K]
300	8913	390	385	17.2×10^{-6}

Table 5. Mechanical properties of the electrodeposited OFHC.

Temperature [K]	Young's Modulus E [GPa]	Poisson's Ratio ν [-]	Yield Stress [MPa]	Ultimate Tensile Strength [MPa]
28	118	0.34	68	413
294	114	0.34	60	208
533	65	0.34	50	145
755	40	0.34	38	80

Table 6. Physical properties of the electrodeposited nickel.

Temperature [K]	Mass Density $[\mathrm{kg/m^3}]$	Thermal Conductivity [W/mK]	Specific Heat [J/kgK]	Thermal Expansion Coefficient [1/K]
300	8913	90	444	12.2×10^{-6}

Table 7. Mechanical properties of the electrodeposited nickel.

Temperature [K]	Young's Modulus E [GPa]	Poisson's Ratio ν [-]	Yield Stress [MPa]	Ultimate Tensile Strength [MPa]
28	193	0.3	344	551

Pressures of the coolant and hot gases were considered as being uniform and equal to 12 and 5 MPa, respectively. A constraint in one node in the axial direction was applied to prevent rigid body motion. The thermal and structural boundary conditions are reported in Figure 7. Combustion gases, coolant bulk temperatures, and their respective heat transfer coefficients varied along the chamber axis, and their values were obtained by computational fluid dynamics (CFD) analyses [25]. In particular, as reported by Ricci et al. [29], two separate CFD simulations were conducted:

- a CFD simulation of the combustion chamber side, accounting for the chemical reactions occurring between the oxidizer and fuel, useful in evaluating the heat transfer coefficients and adiabatic wall temperatures shown in Figure 8;
- a much simpler CFD analysis, since no chemical reaction was involved, to estimate the convective boundary conditions on the cooling channel side.

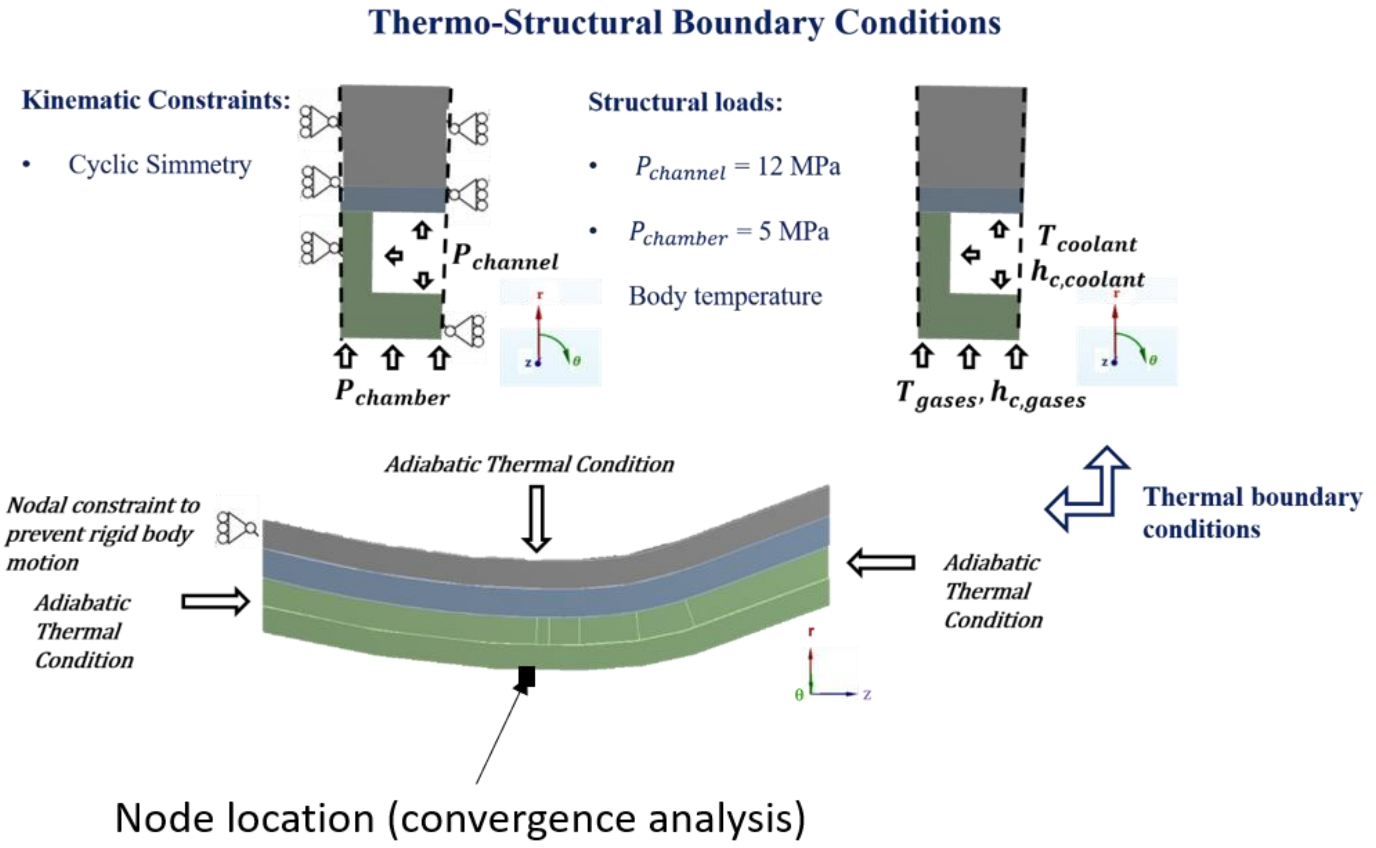

Figure 7. Thermal and structural boundary conditions.

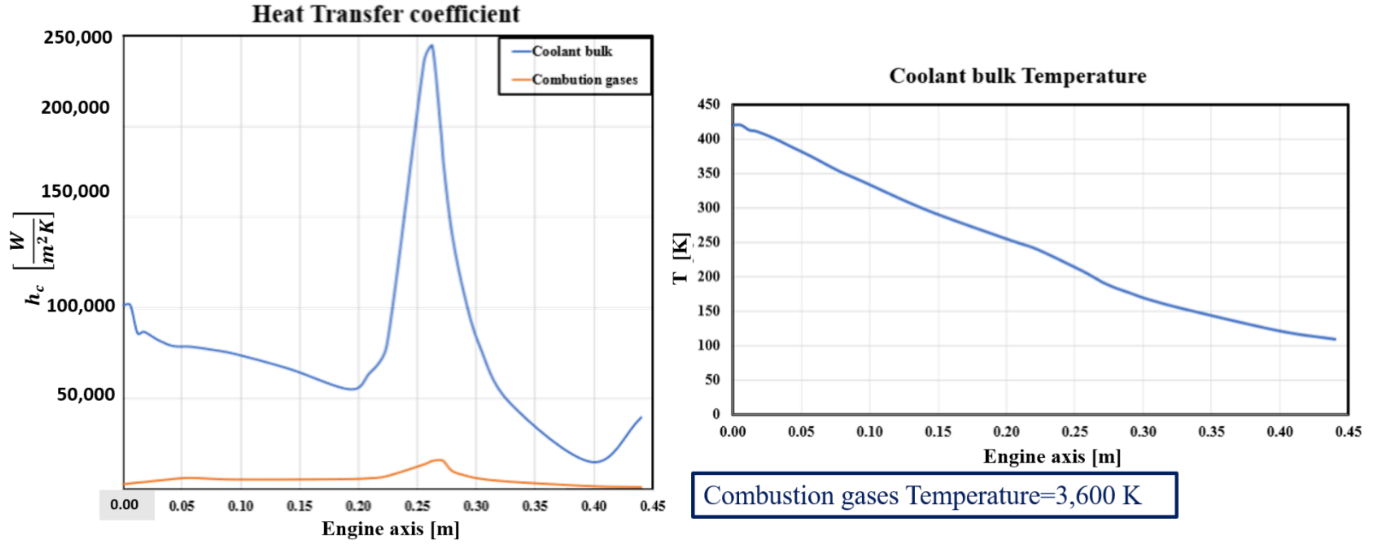

Figure 8. Convective boundary conditions.

A convergence analysis on the FEM mesh was carried out in order to identify the best suited numerical grid to be considered in the analyses, see Figure 9. In particular, in order to illustrate that grid convergence is reached, a node on the internal surface of the cooling channel, where maximum temperatures and plastic strains are envisaged, was selected (see Figure 7).

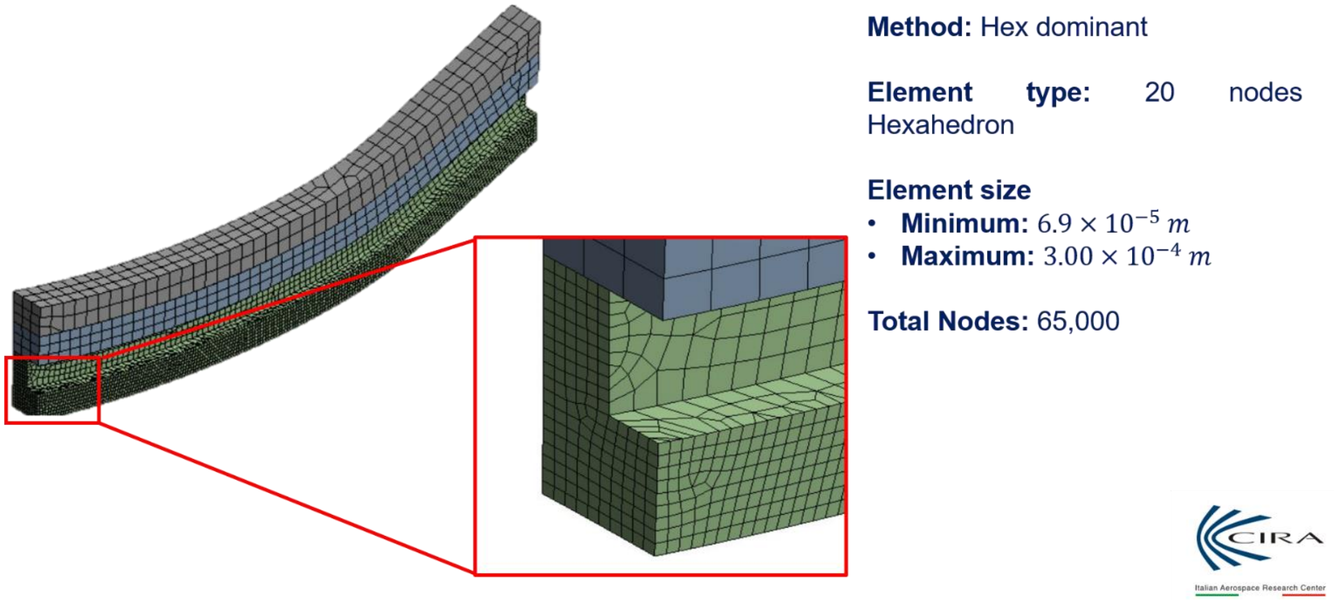

Method: Hex dominant

Element type: 20 nodes Hexahedron

Element size

- **Minimum:** $6.9 \times 10^{-5}\ m$
- **Maximum:** $3.00 \times 10^{-4}\ m$

Total Nodes: 65,000

Figure 9. FEM mesh adopted in the numerical analyses as derived from the convergence analysis.

Plastic strains, creep strains, and temperature values were compared for three grid configurations characterized by four, six and eight elements in the ligament thickness (Figure 9 shows the "eight elements" configuration). In Table 8, the results obtained at the end of the "hot phase" are summarized. The same considerations could be done for other nodes, but for the sake of simplicity, no other results are shown. The computation time needed to perform a thermo-structural analysis with 35 loading cycles is 70 h, adopting a two-core processor.

Table 8. Plastic strains, creep strains, and temperature values at the end of the hot phase.

Number of Elements in the Ligament Thickness [-]	Equivalent Creep Strain [-]	Equivalent Plastic Strain [-]	Temperature [K]
4	0.004896	0.001415	556
6	0.00497	0.001541	556
8	0.00499	0.001599	556

4. Thermal–Structural Cycle Description

Each thermal–structural loading cycle consisted of three sequential phases:

- a purging phase of 3 s, in which the liquid oxygen is injected into the channels to eliminate any waste;
- an ignition transient phase of 3 s, in which the thermal loads are activated;
- the hot phase of 100 s, during which the creep analysis is activated.

No combustion occurs in the thrust chamber in the first three seconds and, therefore, heat convective transfer coefficients and pressures are null. During the ignition phase, combustion occurs, and chamber pressures and convective heat fluxes are generated on the internal surface. The hot phase lasts 100 s, during which creep effects are considered. Table 9 summarizes the load steps and the corresponding time steps Δt adopted in the thermal–structural analyses.

Table 9. Load and time steps considered in the numerical analyses.

Load Steps [-]	Δt [s]	Duration [s]	Phase
10	0.1	1	Purging
5	0.4	2	Purging
15	0.2	3	Ignition Transient
1	100	100	Hot Phase

5. Life Prediction Models

5.1. Ratcheting

With regard to ratcheting, the accumulation of plastic strain ε_{eq} was evaluated by summing up the increment of plastic strain, cycle after cycle:

$$\varepsilon_{eq} = \sum_{\mathrm{i}} \Delta\varepsilon_{eq,i} \tag{9}$$

where the subscript i refers to the ith cycle. The increment in the ith cycle was evaluated by means of the following relationship:

$$\Delta\varepsilon_{eq,i} = \frac{1}{\sqrt{2}(1+\nu)}\sqrt{\left(\Delta\varepsilon_{xx,i}-\Delta\varepsilon_{yy,i}\right)^2+\left(\Delta\varepsilon_{yy,i}-\Delta\varepsilon_{zz,i}\right)^2+\left(\Delta\varepsilon_{zz,i}-\Delta\varepsilon_{xx,i}\right)^2+\frac{3}{2}\left(\Delta\gamma_{xy,i}^2+\Delta\gamma_{yz,i}^2+\Delta\gamma_{zx,i}^2\right)} \tag{10}$$

where $\Delta\varepsilon_{jk,i}$ are evaluated as follows:

$$\Delta\varepsilon_{jk,i} = \varepsilon_{jk,e} - \varepsilon_{jk,b} \tag{11}$$

with $\varepsilon_{jk,e}$ and $\varepsilon_{jk,b}$ representing the plastic strain at the end and at the beginning of the ith cycle ($j = x, y, z$; $k = x, y, z$), respectively.

A significant number of thermal–mechanical cycles was simulated so as to be as accurate as possible in simulating the ratcheting phenomenon and evaluating whether it occurs in the ligament of the thrust chamber. If ratcheting stopped, no contribution of the plastic instability would be considered when evaluating the total usage factor, which sums the effects of creep, fatigue, and ratcheting. On the other hand, if ratcheting increased, with a continuous increment of plastic strains after a significant number of cycles, the service life of the cooling channel N_i associated with plastic instability was evaluated by means of an extrapolation of the obtained plastic strain curve, up to reaching the elongation at break ε_u.

5.2. Creep

The number of cycles to failure N_c, as coming from the creep phenomenon, was evaluated by the following relationship:

$$N_c = \frac{t_{damage}}{t_{cycle}} \tag{12}$$

where t_{damage} is the temperature-dependant rupture time for a steady stress state σ_g and t_{cycle} is the time interval during which the creep phenomenon occurs, see Figure 10 where the experimental curves refer to one-dimensional creep tests at several temperature values [16].

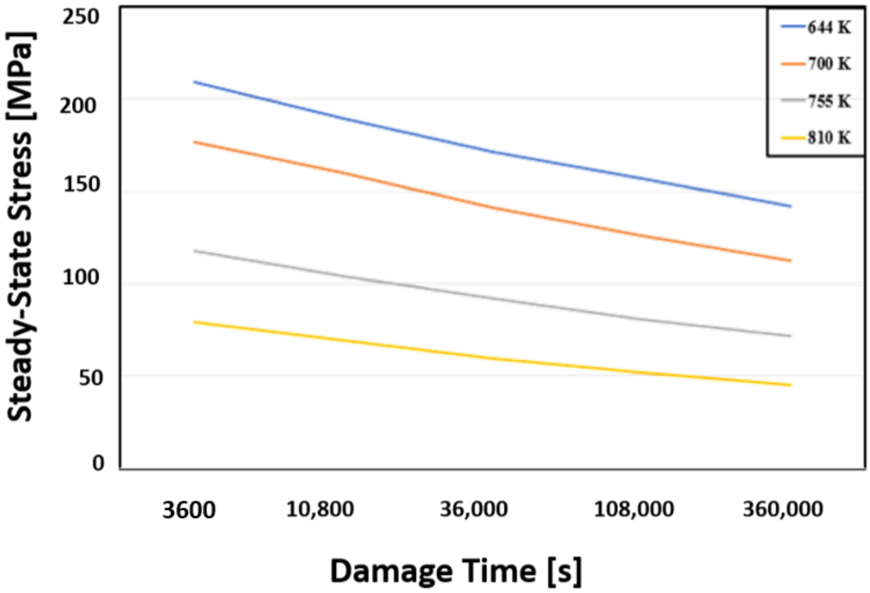

Figure 10. Steady stress vs. damage time [16].

When the pressure in the cooling channel is low, the tangential compressive stresses arising during the hot phase remain compressive up to the end of the creep period; on the contrary, if the pressure in the cooling channel is high, the compressive stresses rapidly relax and become tensile before the end of the hot phase. In the former case, creep is not a potential failure mode, while in the latter, creep rupture damage could occur.

An analytical relationship between the equivalent stress and the number of cycles to failure was used by adopting a multiple linear regression model to fit the CuCrZr experimental creep tests.

The following relationship between steady state stress σ_g and t_{damage} was derived:

$$\sigma_g = A + B\cdot\left(t_{damage}\right)^{-0.28} + C\cdot T \longrightarrow t_{damage} \tag{13}$$

where A, B, and C are constants equal to 596.87 MPa, 799.87 MPa $\mathrm{s}^{0.28}$, and -0.72 MPa/K, respectively. The corresponding coefficient of determination, R^2, is equal to 0.95.

In the next section it will be shown that, in the present test case, compressive stresses do not reverse to tensile ones, making, in such a way, the creep rupture damage not relevant.

5.3. Multiaxial LCF—Non Proportional Loading

Many structural components, such as thrust chambers, experience complex mechanical and thermal loads during their normal working conditions. Such loads can generate multi-axial stress–strain histories and also changes in the principal stress directions. Therefore, fatigue criteria, taking into account both multi-axiality and non-proportional loading, have to be adopted in these cases [18,19,30,31]. Most of the fatigue criteria propose to estimate the value of a uniaxial equivalent strain, which can be considered as being equivalent to the multiaxial strain field. The relationship between this uniaxial equivalent strain and the number of cycles to failure can be obtained through the Basquin–Manson–Coffin relationship [30], represented through the following equation:

$$\varepsilon_{a,eq} = \frac{\sigma'_f - 2\sigma_{n,mean}}{E}\left(2N_f\right)^b + \varepsilon'_f\left(2N_f\right)^c \tag{14}$$

where the fatigue strength coefficient σ'_f and exponent b are parameters of Basquin law, whereas fatigue ductility coefficient ε'_f and exponent c are parameters of Coffin–Manson curve, $\sigma_{n,mean}$ represents the mean stress normal to the maximum shear plane, and $2N_f$ is the number of reversals to failure.

The Wang-Brown criterion is based on a critical plane approach. As demonstrated through numerous experiments [14], fatigue life is usually dominated by crack–growth along either shear planes or tensile planes. This criterion is then based on the idea that shear strains help to nucleate cracks, while normal strain contributes to their growth. The amplitude of the equivalent strain is evaluated according to the following equation:

$$\varepsilon_{a,eq} = \frac{\gamma_{max} + S\delta\varepsilon_n}{1 + v' + S(1 - v')} \tag{15}$$

where γ_{max} is the maximum shear strain amplitude on the critical plane, $\delta\varepsilon_n$ is the normal strain excursion, and v' is the effective Poisson's ratio. The experimental data regarding fatigue tests on CuCrZr coupons are reported in Figure 11 [16]. An analytical relationship between the equivalent strain amplitude and the number of cycles to failure was evaluated by adopting a multiple linear regression model to fit the CuCrZr experimental fatigue tests. Then, the equivalent strain amplitude $\varepsilon_{a,eq}$, estimated according to the Wang-Brown method, was used to estimate the fatigue life according to the following relationship:

$$\varepsilon_{a,eq} = D + H\left(\frac{N_f}{10,000}\right)^{-\frac{0.25T}{1000}} + F\frac{T}{1000} \tag{16}$$

where D, H, and F are constants set as equal to 0.1684, 0.4580, and -0.5987, respectively. The corresponding coefficient of determination, R^2, is equal to 0.96.

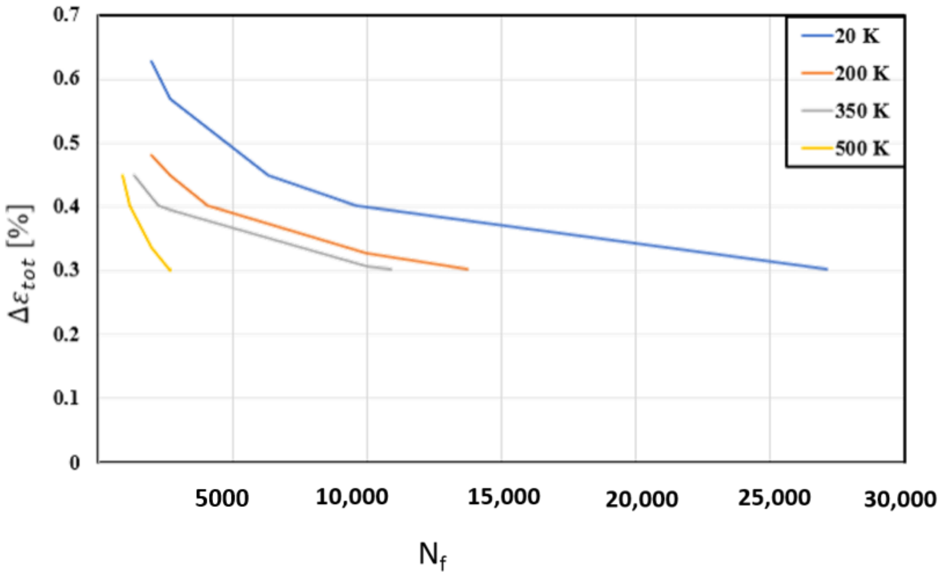

Figure 11. Strain range vs. number of cycles to failure [16].

Finally, a usage factor UF was defined in order to sum the effects of all the described thermal–mechanical phenomena:

$$UF = \frac{1}{N} \tag{17}$$

whereas the total number of cycles prior to failure N_{tot} was evaluated as:

$$N_{tot} = \frac{1}{UF_{tot}} = \frac{1}{UF_i + UF_c + UF_f} = \frac{1}{\frac{1}{N_i} + \frac{1}{N_c} + \frac{1}{N_f}} \tag{18}$$

where UF_i, UF_c, and UF_f are, respectively, the usage factors associated with plastic instability, creep, and low-cycle fatigue.

6. Results and Discussions

The main results of the thermal–mechanical analyses performed on the throat regions are described in this paragraph. Figure 12 shows the temperature and the von Mises stress contour plots for the CuCrZr liner at the end of the purging phase, 0.3 s after starting the ignition phase, and at the end of it. The maximum temperature value of 545 K was still too small for the creep failure occurrence. Indeed, as shown in Figure 12, the lowest temperature value considered in the creep tests is about 100 K greater than the maximum temperature value obtained in the thermal analysis. Furthermore, the ligament compressive stresses in the tangential direction detected in the hot phase remain compressive up to the end of the creep period. Therefore, no creep failure evaluations were needed for the life assessment. On the other hand, creep failure can become dominant when higher thrust levels are required; in fact, higher pressure values are expected in the thrust chamber in this case. However, it is clear that creep relaxation strongly influences the stress–strain response of the structure, leading to an asymmetrical hysteresis curve, which is the cause of an accumulation of tensile plastic strains in the ligament (see Figure 13). Creep effects produce an upward trend of the stress–strain curve, leading to yielding in tension during the following purging phase.

On the other hand, when creep is not modeled, the ligament tensile yielding could not occur and, in turn, a stabilization of the stress–strain curve could be envisaged after a few cycles, leading to a non-conservative estimation of the thrust chamber service life. Therefore, the creep modeling is crucial when studying the ratcheting behavior of the cooling channel. Particularly, primary creep effects, i.e., when creep deformation rate is not constant, are dominant with respect to secondary creep ones, especially in the first ten loading cycles.

With regard to purging and ignition phases, a significant number of time steps were considered (see Table 9). This was due to their very small duration and because very high thermal gradients stresses could be reached especially in initial time intervals. Consequently, a coarse time discretization of these phases could lead to inaccurate results in terms of accumulated plastic strains.

Plastic strains at the end of the ignition phase were reported in Figure 14. It was clear that the tangential strains were dominant with respect to other directions. However, the axial strains were non-negligible, since their maximum value was about one third of the maximum plastic strain in the tangential direction. This demonstrated the need to adopt a multiaxial fatigue criteria.

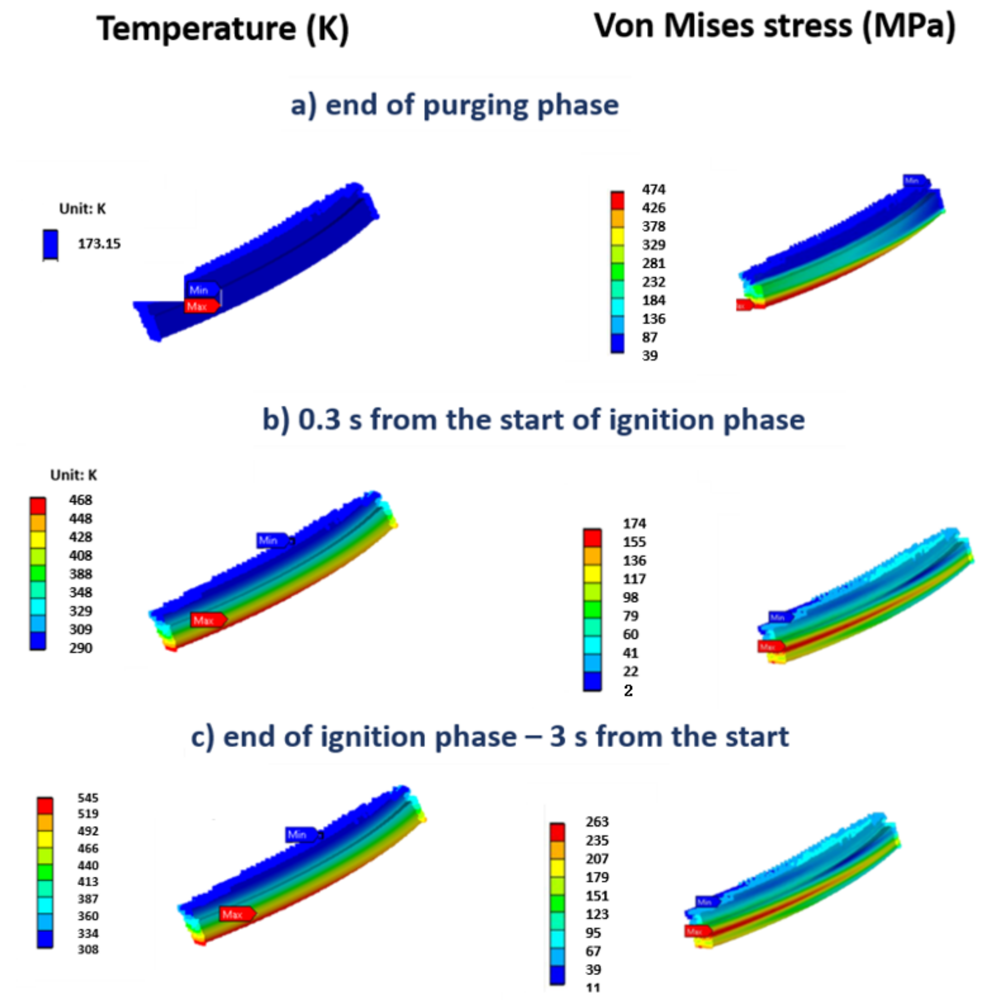

Figure 12. Temperature and von Mises stress contour plots: (**a**) end of purging phase, (**b**) 0.3 s from the start of the ignition phase, (**c**) end of the ignition phase.

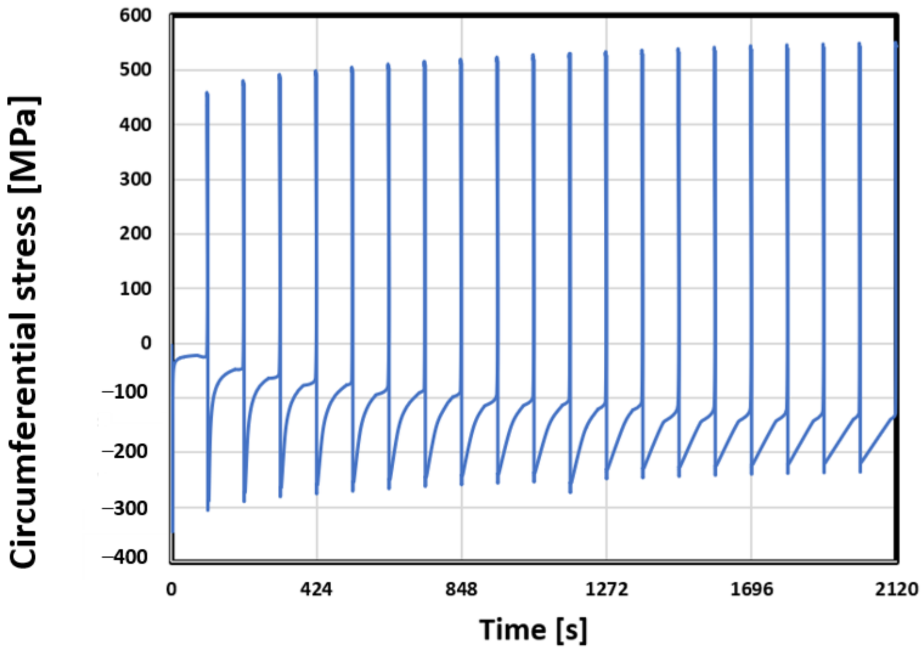

Figure 13. Circumferential stress vs. time.

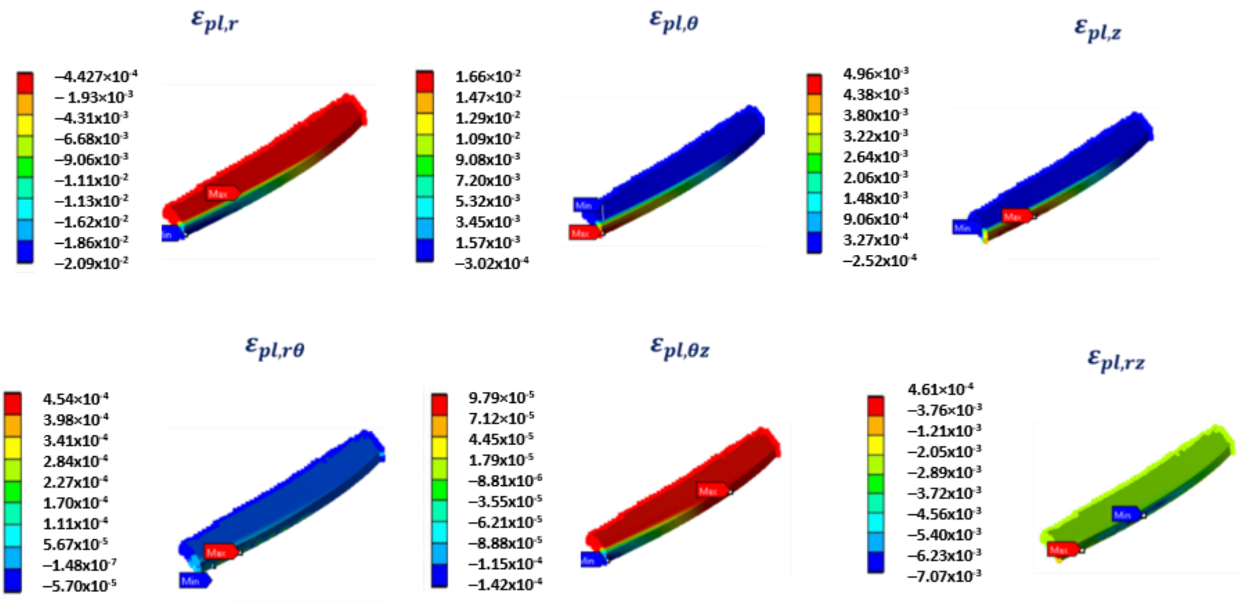

Figure 14. Plastic strains at the end of the ignition phase.

Figures 15 and 16 show that the equivalent plastic strain increased cycle after cycle as a consequence of thermal ratcheting occurring in the ligament. The chosen kinematic hardening model with the three back stresses was capable of simulating ratcheting phenomena even after ten thermal–mechanical cycles. This result is in accordance with the results obtained in [3], showing that at least three Frederick–Armstrong kinematic hardening models should be considered when employing the Chaboche model, in order to properly allow for ratcheting. In fact, if just two hardening models were considered, the shakedown effect would anyway occur after very few cycles. A trendline was extrapolated from the FEM results and a stabilization of the equivalent plastic strains is expected to happen within 30–35 cycles, see Figure 16. As illustrated in Figures 15–17, the increment of plastic strain decreased cycle after cycle. Therefore, it is very likely that a stabilization of the stress–strain curve could occur, even though there is no assurance that it will happen. In this case, LCF could then become the only type of possible failure for the cooling channel. Non-proportional loading effects should be considered; as a matter of fact, the plot of tangential stress vs. tangential strain for a node on the internal surface of the chamber does not depict a straight line passing through the origin of the axes, see Figure 18.

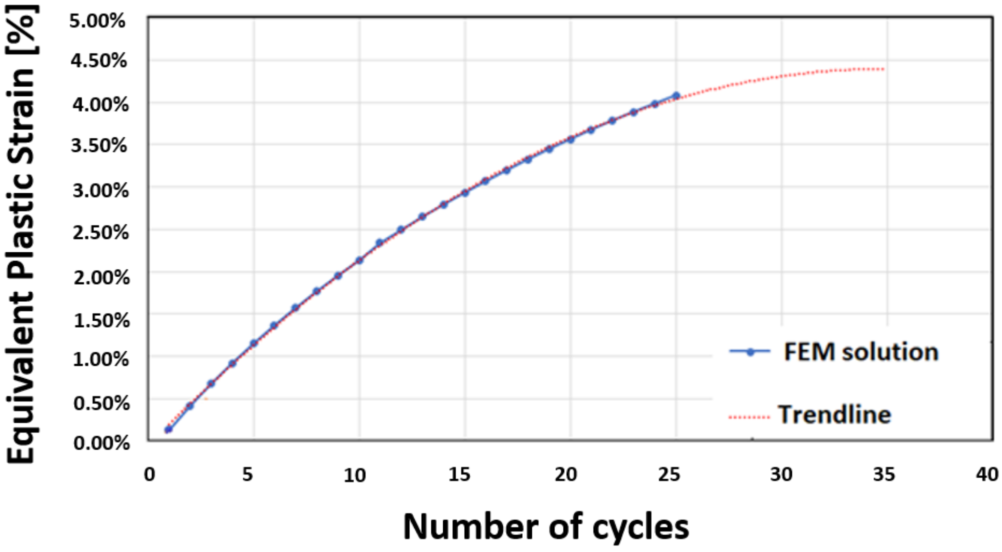

Figure 15. Equivalent plastic strain evolution with number of cycles.

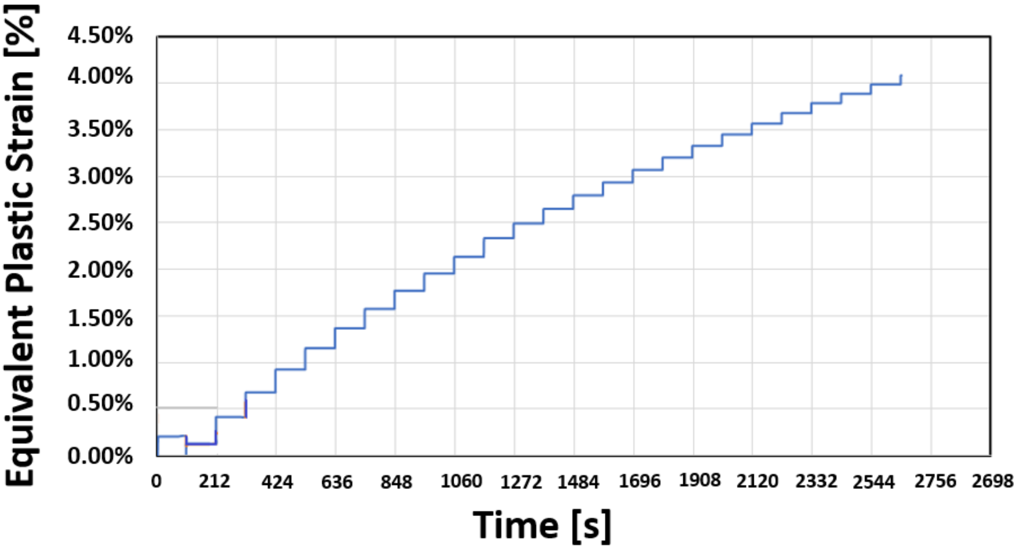

Figure 16. Equivalent plastic strain vs. time—25 cycles.

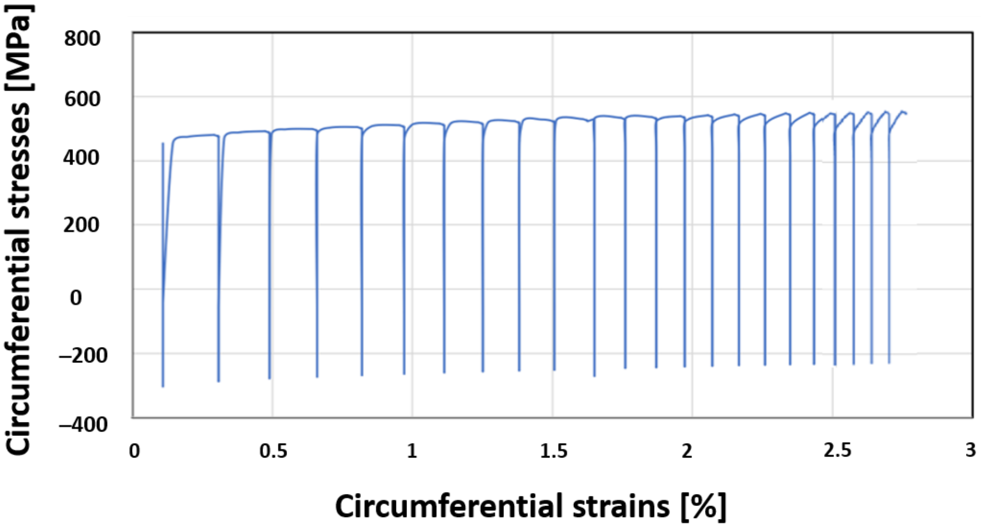

Figure 17. Tangential stress vs. tangential strain.

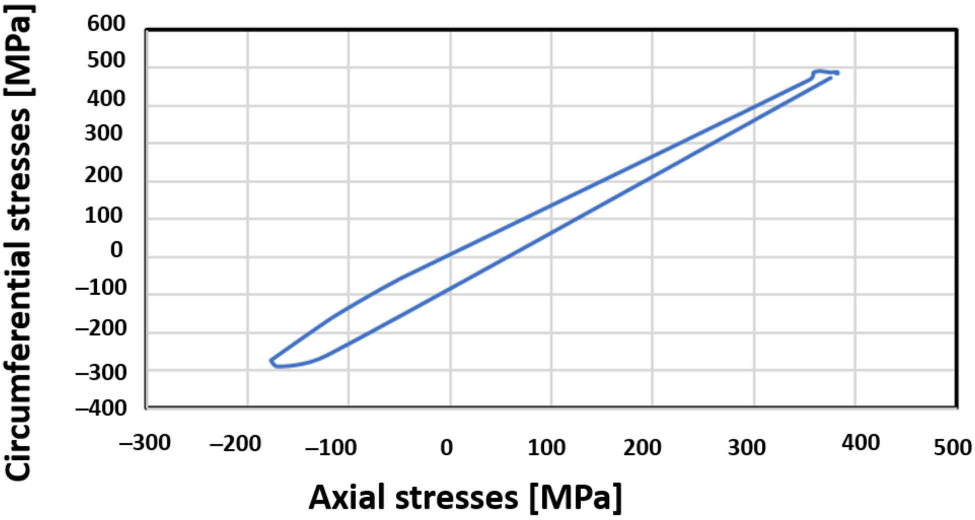

Figure 18. Tangential stress vs. axial stress [MPa].

Finally, fatigue evaluations were carried out adopting the Wang-Brown criterion. Figure 19 shows the service life contour plot obtained employing the abovementioned criterion, highlighting the minimum value of 4776 cycles.

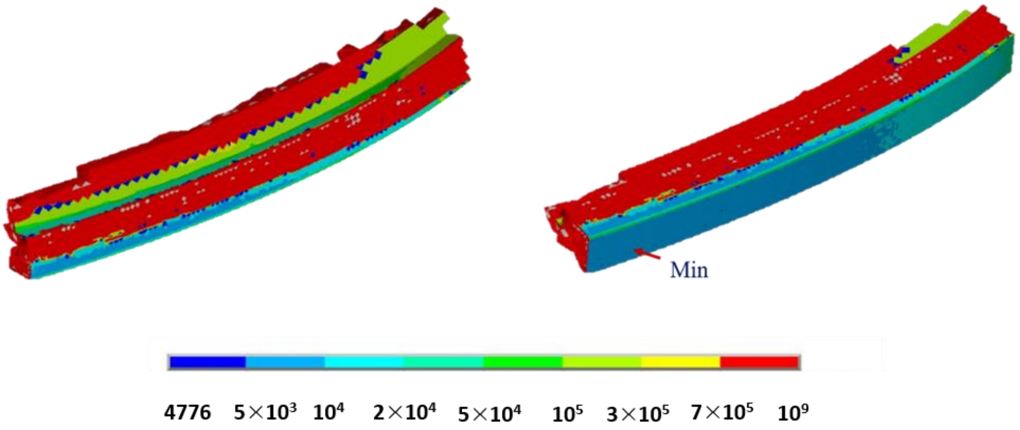

Figure 19. Number of cycles to failure—Wang-Brown criterion.

7. Conclusions

A numerical investigation was conducted with the aim of predicting the service life of a liquid rocket engine thrust chamber. The throat region of the chamber was examined, since the maximum heat fluxes coming from the combustion chamber were expected to occur in this area. A damage model accounting for creep, plastic instability, and multiaxial low-cycle fatigue was adopted to estimate the service life of the chamber.

Results demonstrated that the influence of creep on the thrust chamber failure is negligible with the current geometry, whereas ratcheting is expected to stop after about 30–35 thermal–mechanical loading cycles. Low-cycle fatigue might therefore be the primary cause of failure and, adopting the Wang-Brown multi-axial fatigue criterion, the cooling channel in the throat region was calculated to withstand more than 4000 cycles. This result was consistent with those achieved with similar geometries and loading conditions.

In general, the present work allows us to understand the main factors the designer should consider when sizing a thrust chamber. As an example, the cooling efficiency should be as high as possible in order to reduce temperatures, thermal gradients, and stresses in the throat area, where creep could become a major factor, limiting the service life of the chamber significantly. Furthermore, creep should always be modeled with high fidelity numerical models because it can deeply affect the stress–strain behavior of the component.

As a future activity, submodeling approaches will be adopted in order to obtain more realistic boundary conditions in the cut sections of the local model. A damage model will be also implemented so as to predict the local damage initiation and its further evolution through the material.

Author Contributions: Conceptualization, M.F., R.C., V.G. and M.P.; Data curation, M.F., M.P., V.G. and R.C.; Investigation, M.F., V.G., R.C. and M.P.; Writing—original draft, M.F. and R.C. All authors have read and agreed to the published version of the manuscript.

Funding: This research received no external funding.

Institutional Review Board Statement: Not applicable.

Informed Consent Statement: Not applicable.

Data Availability Statement: Not applicable.

Acknowledgments: This research has been supported by the Italian Ministry of University and Research (MIUR), in the frame of the HYPROB Program.

Conflicts of Interest: The authors declare no conflict of interest.

References

1. Chaboche, J.L. Time-independent constitutive theories for cyclic plasticity. *Int. J. Plast.* **1986**, *2*, 149–188. [CrossRef]
2. Chaboche, J.L. A review of some plasticity and viscoplasticity constitutive theories. *Int. J. Plast.* **2008**, *24*, 1642–1693. [CrossRef]
3. Asraff, A.K.; Sheela, S.; Paul, A.; Mathew, A.; Savithri, S. Cyclic stress analysis of a rocket engine thrust chamber using chaboche, voce and creep constitutive models. *Trans. Indian Inst. Met.* **2016**, *69*, 495–500. [CrossRef]
4. Palma, M.D. Hardening parameters for modelling of CuCrZr and OFHC copper under cyclic loadings. In Proceedings of the 2013 IEEE 25th Symposium on Fusion Engineering (SOFE), San Francisco, CA, USA, 10–14 June 2013; pp. 1–5. [CrossRef]
5. Song, J.; Sun, B. Thermal-structural analysis of regeneratively-cooled thrust chamber wall in reusable LOX/Methane rocket engines. *Chin. J. Aeronaut.* **2017**, *30*, 1043–1053. [CrossRef]
6. Riccius, J.R.; Haidn, O.J.; Zametaev, E.B. Influence of time dependent effects on the estimated life time of liquid rocket combustion chamber walls. In Proceedings of the 40th AIAA/ASME/SAE/ASEE Joint Propulsion Conference and Exhibit, Fort Lauderdale, FL, USA, 11–14 July 2004.
7. Thiede, R.G.; Riccius, J.R.; Reese, S. Life prediction of rocket combustion-chamber-type thermomechanical fatigue panels. *J. Propuls. Power* **2017**, *33*, 1529–1542. [CrossRef]
8. Riccius, J.; Hilsenbeck, M.; Haidn, O. Optimization of geometric parameters of cryogenic liquid rocket combustion chambers. In Proceedings of the 37th Joint Propulsion Conference and Exhibit, Salt Lake City, UT, USA, 8–11 July 2001.
9. You, J.-H.; Miskiewicz, M. Material parameters of copper and CuCrZr alloy for cyclic plasticity at elevated temperatures. *J. Nucl. Mater.* **2008**, *373*, 269–274. [CrossRef]
10. Li, G.; Thomas, B.G.; Stubbins, J.F. Modeling creep and fatigue of copper alloys. *Metall. Mater. Trans. A* **2000**, *31*, 2491–2502. [CrossRef]
11. Ferraiuolo, M.; Russo, V.; Vafai, K. A comparative study of refined and simplified thermo-viscoplastic modeling of a thrust chamber with regenerative cooling. *Int. Commun. Heat Mass Transf.* **2016**, *78*, 155–162. [CrossRef]
12. Ferraiuolo, M.; Petrillo, W.; Riccio, W. On the thermo-structural response of a composite closeout in a regeneratively cooled thrust chamber. *Aerosp. Sci. Technol.* **2017**, *71*, 402–411. [CrossRef]
13. Golan, O.; Arbel, A.; Eliezer, D.; Moreno, D. The applicability of Norton's creep power law and its modified version to a single-crystal superalloy type CMSX-2. *Mater. Sci. Eng. A* **1996**, *216*, 125–130. [CrossRef]
14. Wang, C.H.; Brown, M.W. A path-independent parameter for fatigue under proportional and non-proportional loading. *Fatigue Fract. Eng. Mater. Struct.* **1993**, *16*, 1285–1297. [CrossRef]
15. Ferraiuolo, M.; Leo, M.; Citarella, R. On the adoption of global/local approaches for the thermomechanical analysis and design of liquid rocket engines. *Appl. Sci.* **2020**, *10*, 7664. [CrossRef]
16. Porowski, J.S.; O'Donnell, W.; Badlani, M.L.; Kasraie, B.; Kasper, H.J. Simplified design and life prediction of rocket thrust chambers. *J. Spacecr. Rocket.* **1985**, *22*, 181–187. [CrossRef]
17. Calì, C.; Cricrì, G.; Perrella, M. An advanced creep model allowing for hardening and damage effects. *Strain* **2010**, *46*, 347–357. [CrossRef]
18. Giannella, V.; Citarella, R.; Fellinger, J.; Esposito, R. LCF assessment on heat shield components of nuclear fusion experiment "Wendelstein 7-X" by critical plane criteria. *Procedia Struct. Integr.* **2018**, *8*, 318–331. [CrossRef]
19. Giannella, V.; Citarella, R.; Fellinger, J.; Esposito, R. Multiaxial LCF assessment on plasma facing components of nuclear fusion experiment wendelstein 7-X. In Proceedings of the 23rd Conference of the Italian Association of Theoretical and Applied Mechanics (AIMETA 2017), Salerno, Italy, 4–7 September 2017; Volume 1, pp. 1047–1061.
20. Citarella, R.; Giannella, V.; Vivo, E.; Mazzeo, M. FEM-DBEM approach for crack propagation in a low pressure aeroengine turbine vane segment. *Theor. Appl. Fract. Mech.* **2016**, *86*, 143–152. [CrossRef]
21. Giannella, V.; Vivo, E.; Mazzeo, M.; Citarella, R. FEM-DBEM approach to simulate crack propagation in a turbine vane segment undergoing a fatigue load spectrum. *Procedia Struct. Integr.* **2018**, *12*, 479–491. [CrossRef]
22. Fellinger, J.; Citarella, R.; Giannella, V.; Herold, F.; Stadler, R. Overview of fatigue life assessment of baffles in Wendelstein 7-X. *Fusion Eng. Des.* **2018**, *136*, 292–297. [CrossRef]
23. Sepe, R.; Giannella, V.; Greco, A.; De Luca, A. Fem simulation and experimental tests on the smaw welding of a dissimilar t-joint. *Metals* **2021**, *11*, 1016. [CrossRef]
24. Liu, D.; Sun, B.; Wang, T.; Song, J.; Zhang, J. Thermo-structural analysis of regenerative cooling thrust chamber cylinder segment based on experimental data. *Chin. J. Aeronaut.* **2019**, *33*, 102–115. [CrossRef]
25. Ferraiuolo, M.; Ricci, D.; Battista, F.; Roncioni, P.; Salvatore, V. Thermo-structural and thermo-fluid dynamics analyses supporting the design of the cooling system of a methane liquid rocket engine. In Proceedings of the ASME 2014 International Mechanical Engineering Congress and Exposition, Montreal, QC, Canada, 14–20 November 2014; Volume 1. [CrossRef]
26. Bari, S.; Hassan, T. Anatomy of coupled constitutive models for ratcheting simulation. *Int. J. Plast.* **2000**, *16*, 381–409. [CrossRef]
27. Marzec, J.; Marzec, L.; Martus, P.; Zips, D.; Müller, A.-C. MATLAB®-based fitting method to evaluate survival fractions after multimodal treatment. *Clin. Transl. Radiat. Oncol.* **2018**, *10*, 36–41. [CrossRef]
28. Steel, R.G.D.; Torrie, J.H. *Principles and Procedures of Statistics*; With Special Reference to the Biological Sciences; McGraw-Hill Book Company: New York, NY, USA; Toronto, ON, Canada; London, UK, 1960. [CrossRef]
29. Ricci, D.; Battista, F.; Fragiacomo, M. Numerical investigation on the thermal behaviour of a LOx/LCH4 demonstrator cooling system. *Aerospace* **2021**, *8*, 151. [CrossRef]

30. Itoh, T.; Sakane, M.; Ohsuga, K. Multiaxial low cycle fatigue life under non-proportional loading. *Int. J. Press. Vessel. Pip.* **2013**, *110*, 50–56. [CrossRef]
31. Gowhari-Anaraki, A.R.; Hardy, S.J. Low cycle fatigue life predictions for hollow tubes with axially loaded axisymmetric internal projections. *J. Strain Anal. Eng. Des.* **1991**, *26*, 133–146. [CrossRef]